Unraveling the Quantum Cat
Exploring Master Equation Unravelings

Eric J. Sung*
Program in Applied Mathematics & Department of Mathematics,
University of Arizona, Tucson, AZ 85721, USA
(Dated: December 31, 2024)

Abstract

This report examines the dynamics of open quantum systems with a focus on master equation unravelings and their relevance to Schrödinger cat states. By exploring Poisson and Wiener unravelings, we demonstrate their distinct stochastic dynamics while maintaining consistency with the Lindblad master equation on average. The work introduces foundational concepts such as coherent states, field oscillators, and beam-splitter transformations, which are pivotal for understanding macroscopic quantum superpositions. Experimental techniques, particularly homodyne detection, are highlighted for their role in reconstructing field quadratures and Wigner functions, offering a practical approach to distinguishing between unravelings. Special attention is given to the experimental realization of Schrödinger cat states in cavity quantum electrodynamics, emphasizing their significance in bridging quantum and classical phenomena. The report concludes with a discussion on future research directions, including experimental validation of theoretical predictions and the application of unravelings to quantum technologies such as error correction and sensing.

* jsung1@arizona.edu

Contents

1 Introduction 4

2 Open Quantum Systems 4
- 2.1 Open Quantum Systems . . . 4
- 2.2 Lindblad Master Equation . . . 5

3 Unraveling the Master Equation 6
- 3.1 Quantum Jump (Monte Carlo) Method . . . 6
- 3.2 Poisson Unraveling . . . 10
- 3.3 Wiener Unraveling . . . 12

4 Schrödinger Cat States 14
- 4.1 Definition and Construction of Schrödinger Cat States . . . 14
- 4.2 Properties and Applications . . . 14
- 4.3 Generalization to Multi-Component Cat States . . . 15
- 4.4 Experimental Realization . . . 15

5 Homodyne Detection 16

6 Unraveling the Cat 17
- 6.1 Case Study: Homodyne Cat State Measurement . . . 17
- 6.2 The Jumping Cat: Poisson Unraveling . . . 19
- 6.3 The Randomly Walking Cat: Wiener Unraveling . . . 21
- 6.4 Comparing the Unravelings . . . 23

7 Outlook 26
- 7.1 Discerning Between the Jump and Continuous Walk . . . 26

Appendix **26**

A Field Oscillators 27

B Coherent States 28
- B1 Definition . . . 28
- B2 Normalization of Coherent States . . . 29
- B3 Displacement Operator Representation . . . 29
- B4 Properties of Coherent States . . . 29
- B5 Coherent States in Phase Space . . . 30

C Coupled Harmonic Oscillators 30

D Quantum Action of the Beam-Splitter 31
- D1 Beam-Splitter Transformation . . . 31
- D2 Interaction Hamiltonian and Heisenberg Picture . . . 32
- D3 Schrödinger Picture and State Transformation . . . 33

References 34

1 Introduction

In this paper, we provide a detailed description of master equation unravelings and their application to Schrödinger cat states in the context of quantum optics. The study of open quantum systems forms the foundation of this discussion, as it provides the theoretical framework for understanding how quantum systems interact with their environment. By exploring both Poisson and Wiener unravelings, we aim to highlight their unique contributions to modeling the dynamics of open quantum systems.

This paper is designed to be as self-contained as possible, offering foundational insights into coherent states, field oscillators, and the quantum mechanics of beam splitters. These concepts are essential for understanding Schrödinger cat states and their significance in bridging the classical-quantum divide. Schrödinger cat states, often regarded as superpositions of macroscopically distinct quantum states, provide an ideal platform for studying decoherence and the quantum-to-classical transition.

We assume the reader has knowledge of quantum mechanics and electrodynamics at the level of Sakurai [1] and Jackson [2], respectively. The mathematical and physical tools required to comprehend unravelings, such as stochastic differential equations, density matrix formalism, and quantum trajectory theory, are introduced where necessary.

2 Open Quantum Systems

2.1. Open Quantum Systems

Open quantum systems are systems that interact with their surrounding environment, leading to an exchange of energy and information. Unlike closed systems, whose dynamics are governed solely by the Schrödinger equation, open quantum systems must account for the effects of this interaction. Mathematically, the total system is described in terms of three key components: the system of interest, the environment, and their interaction, as depicted in Figure 1.

The total Hilbert space $\mathcal{H}_T$ is the tensor product of the system Hilbert space $\mathcal{H}_A$ and the environment Hilbert space $\mathcal{H}_E$:

$$\mathcal{H}_T = \mathcal{H}_A \otimes \mathcal{H}_E. \tag{2.1}$$

The dynamics of the total system are governed by the total Hamiltonian H_T:

$$H_T = H_A \otimes \mathbb{I}_E + \mathbb{I}_A \otimes H_E + H_{AE}, \tag{2.2}$$

where H_A, H_E, and H_{AE} are the Hamiltonians of the system, environment, and their interaction, respectively. The density matrix of the total system, ρ_T, evolves according to the Liouville-von Neumann equation:

$$\frac{\partial \rho_T}{\partial t} = -\frac{i}{\hbar}[H_T, \rho_T]. \tag{2.3}$$

For practical purposes, we are often interested in the reduced dynamics of the system ρ_A,

which is obtained by tracing out the environmental degrees of freedom:

$$\rho_A = \mathrm{Tr}_E(\rho_T). \tag{2.4}$$

The challenge lies in describing ρ_A's evolution, which is influenced by the interaction H_{AE}. The reduced dynamics are non-unitary and often characterized by decoherence and dissipation, essential phenomena in understanding the transition from quantum to classical behavior [3, 4].

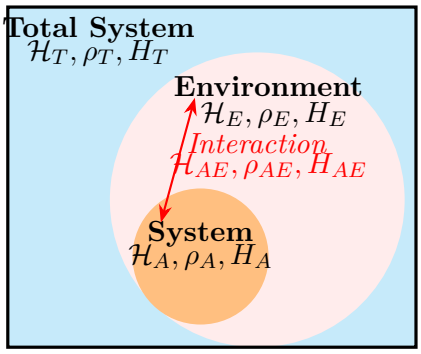

FIG. 1. Open quantum system interacting with its environment.

2.2. Lindblad Master Equation

To describe the reduced dynamics of an open quantum system under Markovian assumptions, the Lindblad master equation is commonly used. This equation provides a mathematical framework for systems weakly coupled to memoryless environments [3]:

$$\frac{\partial \rho}{\partial t} = -\frac{i}{\hbar}[H, \rho] + \sum_i \gamma_i \left(L_i \rho L_i^\dagger - \frac{1}{2}\{L_i^\dagger L_i, \rho\} \right), \tag{2.5}$$

where $\{A, B\} = AB + BA$ is the anticommutator. In this equation, the first term represents the coherent evolution of the system governed by the Hamiltonian H, which includes contributions from the system itself and its interaction with the environment. The second term, often referred to as the dissipator, encapsulates the irreversible effects of the environment on the system. These effects include processes such as energy loss, dephasing, and thermalization.

The operators L_i, known as Lindblad operators, describe specific channels of dissipation or decoherence. For example, in optical systems, they may represent photon emission or absorption processes [4]. The coefficients γ_i denote the rates at which these processes occur and depend on the properties of the environment and its coupling to the system.

One of the key strengths of the Lindblad master equation is its guarantee of complete positivity and trace preservation for the system's density matrix ρ. This ensures that the reduced density matrix remains a valid physical state throughout its evolution. The Lindblad equation has been widely applied to study phenomena such as spontaneous emission in atomic systems, energy transfer in biological molecules, and decoherence in quantum computing platforms [3].

The insights provided by the Lindblad framework are invaluable for understanding how

quantum systems lose coherence and transition to classical behavior, bridging fundamental quantum mechanics and practical applications in quantum technologies.

3 Unraveling the Master Equation

Understanding the dynamics of open quantum systems often requires solving the Lindblad master equation. However, the density matrix representation of a quantum system involves N_A^2 elements, where N_A is the dimension of the system's Hilbert space. This quadratic scaling quickly renders numerical simulations infeasible for large systems, even on powerful supercomputers. To overcome this challenge, alternative methods focus on unraveling the master equation, which shifts the computational burden from handling the density matrix to simulating individual quantum trajectories.

Unraveling the master equation provides not only computational advantages but also deeper physical insights into open quantum systems. Instead of describing the ensemble evolution of the density matrix, unraveling models the stochastic evolution of pure states, enabling a trajectory-by-trajectory understanding of the system's dynamics. These methods are particularly valuable in connecting theoretical predictions with experimental observations, such as quantum jumps in atomic systems or photon emissions in optical cavities [3, 4].

By employing unraveling techniques, we can recover the Lindblad dynamics as the statistical average over many simulated trajectories. This approach bridges the density matrix formalism and single-state dynamics, offering both computational efficiency and an intuitive understanding of the interplay between coherence and dissipation in quantum systems.

3.1. Quantum Jump (Monte Carlo) Method

Suppose we have a system A coupled to the environment E. Let B be the environmental simulator of E. Let H_A, H_B, and H_{AB} (H_{AE}) be the Hamiltonians of A, B, and AB (AE), respectively. If ρ_A is the density operator of A, ρ_A is the partial trace of ρ_{A+B} and ρ_A obeys the Lindblad master equation. In practice, the Lindblad master equation cannot be solved analytically thus numerical schemes must be implemented. Recall that the number of elements of the density matrix ρ_A is N_A^2, namely, the square of the dimension of the Hilbert space. It is clear that computation of ρ_A quickly becomes unfeasible even for the most powerful supercomputers due to the $\mathcal{O}(N_A^2)$ complexity of calculating ρ_A. However, the wave function ψ_A involves only N_A variables thus it is favorable to focus on the Hamiltonian evolution of the wave function. This radically changes how we describe the system from calculating ensemble averages to calculating single trajectories.

We describe how this method works. Suppose that at time $t = 0$, system A is in the pure state $|\phi^{(A)}(0)\rangle$. Let $|\phi^{(A)}(t)\rangle$ be the state of A at some time t. Suppose that system B is initially in the reference state $|0^B\rangle$ at time t. We split the time interval in increments of τ where $\tau_c \ll \tau \ll T_r$. After the first time step τ, measure some observable O_B to see if a quantum jump occurred and which one it was. The probability of no jump occurring is

$$p_0 = 1 - \tau \sum_{\mu \neq 0} \langle \phi^{(A)} | L_\mu^\dagger L_\mu | \phi^{(A)} \rangle \,. \tag{3.1}$$

If a jump does occur, it occurs with probability

$$p_\mu = \tau \langle \phi^{(A)} | L_\mu^\dagger L_\mu | \phi^{(A)} \rangle . \tag{3.2}$$

Record the result of the obtained value. After this measurement, A is then projected onto a new (normalized) state

$$|\phi^{(A)}(t)\rangle \to |\phi^{(A)}(t+\tau)\rangle , \tag{3.3}$$

where

$$|\phi^{(A)}(t+\tau)\rangle = \begin{cases} \frac{L_\mu}{\sqrt{p_\mu/\tau}} |\phi^{(A)}(t)\rangle , & \text{Jump,} \\ \frac{1-iH_{\text{eff}}\tau/\hbar}{\sqrt{p_0}} |\phi^{(A)}(t)\rangle , & \text{No-Jump,} \end{cases} \tag{3.4}$$

and $H_{\text{eff}} = H_A - i\hbar J$ is the non-Hermitian, effective Hamiltonian with

$$J = \frac{1}{2} \sum_{\mu \neq 0} L_\mu^\dagger L_\mu . \tag{3.5}$$

Then we re-initialize B back to its reference state $|0^{(B)}\rangle$, which is justified by the fact that the entanglement of A with the real environment E can be neglected by the Markovian approximation. Repeat this process step by step which eventually yields the total evolution. This process is stated algorithmically as follows:

Algorithm 1 Quantum Monte Carlo Trajectory

Input: Initial State at time t: $|\phi^{(A)}(t)\rangle$, System Hamiltonian: H_A, Jump Operators: L_μ where $\mu \in \{1, 2, \ldots, N_K - 1\}$, Max Iterations: $N_{\max}$, Time Step: τ

$J \leftarrow \frac{1}{2} \sum_{\mu \neq 0} L_\mu^\dagger L_\mu$
$H_{\text{eff}} \leftarrow H_A - i\hbar J$
$|\phi^{(A)}\rangle \leftarrow |\phi^{(A)}(t)\rangle$ ▷ Initialize the state
for $j = 1$ to $N_{\max}$ **do**
    $p_0 \leftarrow 1 - \tau \sum_{\mu \neq 0} \langle \phi^{(A)} | L_\mu^\dagger L_\mu | \phi^{(A)} \rangle$ ▷ No-jump probability
    for $\mu \in \{1, 2, \ldots, N_K - 1\}$ **do**
        $p_\mu \leftarrow \tau \langle \phi^{(A)} | L_\mu^\dagger L_\mu | \phi^{(A)} \rangle$ ▷ Jump probabilities
    end for
    Draw random $r \in [0, 1]$ uniformly
    if $r < p_0$ **then** ▷ No-jump case
        $|\phi^{(A)}(\tau)\rangle \leftarrow \frac{1-iH_{\text{eff}}\tau/\hbar}{\sqrt{p_0}} |\phi^{(A)}\rangle$
    else ▷ Jump case
        $\nu \leftarrow \min \left\{ \nu \in \mathbb{Z}^+ \cup \{0\} : r < \sum_{\mu=0}^{\nu} p_\mu \right\}$
        $|\phi^{(A)}(\tau)\rangle \leftarrow \frac{L_\nu}{\sqrt{p_\nu/\tau}} |\phi^{(A)}\rangle$
    end if
    $|\phi^{(A)}\rangle \leftarrow |\phi^{(A)}(\tau)\rangle$ ▷ New initial state
end for

Output: $|\phi^{(A)}\rangle$

We see from Algorithm 1 that many individual quantum trajectories $|\phi_j^{(A)}(t)\rangle$ are constructed from the same initial state. To see the equivalence of the quantum Monte Carlo method with the Lindblad master equation, let

$$\Pi_j(t) = |\phi_j^{(A)}(t)\rangle \langle \phi_j^{(A)}(t)|, \tag{3.6}$$

be the projector of the j-th trajectory. Then the average of the projectors is

$$\overline{\Pi}(t) = \sum_{j=0} p_j \Pi_j(t) = \sum_{j=0} p_j |\phi_j^{(A)}(t)\rangle \langle \phi_j^{(A)}(t)|. \tag{3.7}$$

To find the time evolution of $\overline{\Pi}(t)$, namely,

$$\frac{d\overline{\Pi}}{dt} = \lim_{\tau\to 0}\left(\frac{\overline{\Pi}(t+\tau) - \overline{\Pi}(t)}{\tau}\right). \tag{3.8}$$

To evaluate $\overline{\Pi}(t+\tau)$, recall that $\overline{\Pi}(t+\tau)$ consists of the contributions from the no-jump and jump cases weighted by their probabilities p_0 and p_μ, respectively,

$$\begin{aligned}\overline{\Pi}(t+\tau) &= p_0 \overline{\Pi}^{no-jump}(t+\tau) + (1-p_0)\overline{\Pi}^{jump}(t+\tau) \\ &= p_0 \overline{\Pi}^{no-jump}(t+\tau) + p_\mu \overline{\Pi}^{jump}(t+\tau).\end{aligned} \tag{3.9}$$

For the no-jump case, recall that the time evolution of $|\phi_j^{(A)}(t)\rangle$ is governed by the non-Hermitian, effective Hamiltonian $H_{\text{eff}} = H_A - i\hbar J$. Thus we have

$$|\phi_j^{(A)}(t+\tau)\rangle = \frac{1 - iH_{\text{eff}}\tau/\hbar}{\sqrt{p_0}} |\phi_j^{(A)}(t)\rangle. \tag{3.10}$$

Then we have

$$\begin{aligned}\Pi_j^{no-jump}(t+\tau) &= |\phi_j^{(A)}(t+\tau)\rangle \langle \phi_j^{(A)}(t+\tau)| \\ &= \frac{1}{p_0}\left(1 - iH_{\text{eff}}\tau/\hbar\right) |\phi_j^{(A)}(t)\rangle \langle \phi_j^{(A)}(t)| \left(1 + iH_e^\dagger \tau/\hbar\right) \\ &= \frac{1}{p_0}\left(1 - iH_{\text{eff}}\tau/\hbar\right) \Pi_j(t) \left(1 + iH_e^\dagger \tau/\hbar\right) \\ &= \frac{1}{p_0}\left(\Pi_j(t) - \frac{i\tau}{\hbar}[H_A, \Pi_j(t)] - \tau\left(\Pi_j(t)J + J\Pi_j(t)\right) + \frac{\tau^2}{\hbar^2} H_{\text{eff}}\Pi_j(t)H_e^\dagger\right) \\ &= \frac{1}{p_0}\left(\Pi_j(t) - \frac{i\tau}{\hbar}[H_A, \Pi_j(t)] - \frac{\tau}{2}\sum_{\mu\neq 0}\left(\Pi_j(t)L_\mu^\dagger L_\mu + L_\mu^\dagger L_\mu \Pi_j(t)\right)\right. \\ &\left. + \frac{\tau^2}{\hbar^2} H_{\text{eff}}\Pi_j(t)H_e^\dagger\right).\end{aligned} \tag{3.11}$$

Averaging then yields

$$\begin{aligned}\overline{\Pi}^{no-jump}(t+\tau) &= \sum_{j=0} p_j \Pi_j^{no-jump}(t+\tau) \\ &= \frac{1}{p_0}\left(\overline{\Pi}(t) - \frac{i\tau}{\hbar}[H_A, \overline{\Pi}(t)] - \frac{\tau}{2}\sum_{\mu\neq 0}\left(\overline{\Pi}(t)L_\mu^\dagger L_\mu + L_\mu^\dagger L_\mu \overline{\Pi}(t)\right)\right. \\ &\left. + \frac{\tau^2}{\hbar^2} H_{\text{eff}}\overline{\Pi}(t) H_e^\dagger\right). \end{aligned} \tag{3.12}$$

For the jump case, recall that

$$|\phi_j^{(A)}(t+\tau)\rangle = \frac{L_\mu}{\sqrt{p_\mu/\tau}}\,|\phi_j^{(A)}(t)\rangle\,. \tag{3.13}$$

Thus we get

$$\Pi_j^{jump}(t+\tau) = \frac{\tau}{p_\mu} L_\mu \Pi_j(t) L_\mu^\dagger. \tag{3.14}$$

Averaging then yields

$$\begin{aligned}\overline{\Pi}^{jump}(t+\tau) &= \sum_{j=0} p_j \Pi_j^{jump}(t+\tau) \\ &= \frac{\tau}{p_\mu} L_\mu \overline{\Pi}(t) L_\mu^\dagger. \end{aligned} \tag{3.15}$$

Thus we have

$$\begin{aligned}\overline{\Pi}(t+\tau) &= p_0 \overline{\Pi}^{no-jump}(t+\tau) + p_\mu \overline{\Pi}^{jump}(t+\tau) \\ &= \overline{\Pi}(t) - \frac{i\tau}{\hbar}[H_A, \overline{\Pi}(t)] + \tau\sum_{\mu\neq 0}\left(L_\mu \overline{\Pi}(t) L_\mu^\dagger - \frac{1}{2}\overline{\Pi}(t)L_\mu^\dagger L_\mu - \frac{1}{2}L_\mu^\dagger L_\mu \overline{\Pi}(t)\right) \\ &+ \frac{\tau^2}{\hbar^2} H_{\text{eff}}\overline{\Pi}(t) H_e^\dagger. \end{aligned} \tag{3.16}$$

Then we get

$$\begin{aligned}\frac{d\overline{\Pi}}{dt} &= \lim_{\tau\to 0}\left(\frac{\overline{\Pi}(t+\tau) - \overline{\Pi}(t)}{\tau}\right) \\ &= \overline{\Pi}(t) - \frac{i}{\hbar}[H_A, \overline{\Pi}(t)] + \sum_{\mu\neq 0}\left(L_\mu \overline{\Pi}(t) L_\mu^\dagger - \frac{1}{2}\overline{\Pi}(t)L_\mu^\dagger L_\mu - \frac{1}{2}L_\mu^\dagger L_\mu \overline{\Pi}(t)\right). \end{aligned} \tag{3.17}$$

Thus the time evolution of $\overline{\Pi}$ is that of the Lindblad form of the master equation. Since by construction $\rho_A(0) = \overline{\Pi}(0)$, we have that $\rho_A(t)$ and $\overline{\Pi}(t)$ coincide at all times, namely,

$$\rho_A(t) = \overline{\Pi}(t). \tag{3.18}$$

Therefore, the Lindblad and Monte Carlo methods are equivalent.

Besides the numerical advantage, the Monte Carlo method provides a physically different interpretation over the density matrix approach. The density matrix approach describes the quantum average over an ensemble of identical copies of the same experiment. Meanwhile, the Monte Carlo method focuses on the individual trajectories of a single realization of the experiment. It is fascinating that two radically different approaches yield the same results. Coupled with the real experimental developments in actually observing quantum trajectories, the Monte Carlo method provides another way of studying decoherence.

One must be cautious in interpreting the physics of the trajectory method. To illustrate this, suppose that there exists a unitary transformation T in the Hilbert space of A such that

$$T\mathcal{D}[\rho_A]T^\dagger = \mathcal{D}[T\rho_A T^\dagger]. \tag{3.19}$$

where

$$\mathcal{D}[\rho_A] = \sum_\mu L_\mu \rho_A L_\mu^\dagger - \frac{1}{2}L_\mu^\dagger L_\mu \rho_A - \frac{1}{2}\rho_A L_\mu^\dagger L_\mu, \tag{3.20}$$

is the dissipator of the master equation [5]. Then we can define the new jump operators $A_\mu = T^\dagger L_\mu T$ which leads to

$$\begin{aligned}
&\sum_\mu A_\mu \rho_A A_\mu^\dagger - \frac{1}{2}A_\mu^\dagger A_\mu \rho_A - \frac{1}{2}\rho_A A_\mu^\dagger A_\mu \\
&= \sum_\mu T^\dagger L_\mu T \rho_A T^\dagger L_\mu T - \frac{1}{2}T^\dagger L_\mu^\dagger T T^\dagger L_\mu T \rho_A T^\dagger T - \frac{1}{2}T^\dagger T \rho_A T^\dagger L_\mu^\dagger T T^\dagger L_\mu T \\
&= \sum_\mu T^\dagger L_\mu (T\rho_A T^\dagger) L_\mu T - \frac{1}{2}T^\dagger L_\mu^\dagger L_\mu (T\rho_A T^\dagger) T - \frac{1}{2}T^\dagger (T\rho_A T^\dagger) L_\mu^\dagger L_\mu T \\
&= T^\dagger \left[\sum_\mu L_\mu (T\rho_A T^\dagger) L_\mu - \frac{1}{2}L_\mu^\dagger L_\mu (T\rho_A T^\dagger) - \frac{1}{2}(T\rho_A T^\dagger) L_\mu^\dagger L_\mu \right] T \\
&= T^\dagger \mathcal{D}[T\rho_A T^\dagger] T \\
&= \mathcal{D}[\rho_A].
\end{aligned} \tag{3.21}$$

Thus the same physics is reproduced with the different jump operator A_μ. In the context of using the quantum trajectory method purely for numerical computations, the choice of the jump operator is typically the one that provides the fastest convergence rate of the algorithm. In order to give a physical interpretation of an individual trajectory, the action of the jump operators must be able to be associated with measurable properties of the environment.

3.2. Poisson Unraveling

The Poisson unraveling describes the dynamics of an open quantum system in terms of stochastic processes where discrete jumps are superimposed on deterministic evolution. This section provides a detailed derivation of the stochastic differential equation (SDE) for Poisson unraveling, starting from the quantum jump (Monte Carlo) method.

The evolution of the system is described by the Lindblad master equation [3, 6]:

$$\frac{\partial \rho}{\partial t} = -\frac{i}{\hbar}[H, \rho] + \sum_{\mu} \left(L_\mu \rho L_\mu^\dagger - \frac{1}{2}\{L_\mu^\dagger L_\mu, \rho\} \right), \tag{3.22}$$

where H is the Hermitian system Hamiltonian and L_μ are the Lindblad operators representing dissipative processes. Our goal is to derive the equivalent stochastic differential equation that describes the evolution of the wave function $|\psi(t)\rangle$ under Poisson unraveling.

We begin by introducing the non-Hermitian effective Hamiltonian, which governs the deterministic, no-jump evolution of the wave function [6, 7]:

$$H_{\text{eff}} = H - \frac{i\hbar}{2} \sum_{\mu} L_\mu^\dagger L_\mu. \tag{3.23}$$

This effective Hamiltonian accounts for the influence of dissipation without explicitly modeling jumps. Between jumps, the wave function evolves as:

$$\frac{d}{dt} |\psi(t)\rangle = -\frac{i}{\hbar} H_{\text{eff}} |\psi(t)\rangle . \tag{3.24}$$

Over a short time interval δt, the no-jump evolution is:

$$|\psi(t + \delta t)\rangle = \frac{1 - \frac{iH_{\text{eff}}\delta t}{\hbar}}{\sqrt{1 - \delta P_{\text{jump}}}} |\psi(t)\rangle , \tag{3.25}$$

where δP_{jump} is the probability of a jump occurring in $[t, t + \delta t]$.

The probability of a jump occurring in a small time interval δt is given by [7]:

$$\delta P_{\text{jump}} = \delta t \sum_{\mu} \langle L_\mu^\dagger L_\mu \rangle_{\psi_t} , \tag{3.26}$$

where $\langle \cdot \rangle_{\psi_t} \equiv \langle \psi(t)| \cdot |\psi(t)\rangle$. If a jump occurs, the probability of the jump being of type μ is:

$$P_\mu = \frac{\langle L_\mu^\dagger L_\mu \rangle_{\psi_t}}{\sum_\nu \langle L_\mu^\dagger L_\mu \rangle_{\psi_t}^{1/2}}. \tag{3.27}$$

Following a jump, the wave function updates to [6]:

$$|\psi(t + \delta t)\rangle = \frac{L_\mu |\psi(t)\rangle}{\langle L_\mu^\dagger L_\mu \rangle_{\psi_t}^{1/2}}. \tag{3.28}$$

To describe both jump and no-jump dynamics in a unified framework, we introduce stochastic processes $dN_\mu(t)$ representing the occurrence of jumps. The increments $dN_\mu(t)$ satisfy:

$$dN_\mu(t) = \begin{cases} 1 & \text{if a jump of type } \mu \text{ occurs in } [t, t + dt], \\ 0 & \text{otherwise.} \end{cases} \tag{3.29}$$

The expectation value of $dN_\mu(t)$ is:

$$\mathbb{E}[dN_\mu(t)] = \langle L_\mu^\dagger L_\mu \rangle_{\psi_t} \, dt. \tag{3.30}$$

The evolution of the wave function can now be written as a stochastic differential equation (SDE) [6, 7]:

$$d\,|\psi(t)\rangle = -\frac{i}{\hbar} H_{\text{eff}}\,|\psi(t)\rangle\,dt + \sum_\mu \left(\frac{L_\mu}{\langle L_\mu^\dagger L_\mu \rangle_{\psi_t}^{1/2}} - I \right) |\psi(t)\rangle\, dN_\mu(t). \tag{3.31}$$

Combining the deterministic and stochastic terms, the full SDE for the Poisson unraveling is:

$$d\,|\psi(t)\rangle = -\left(\frac{i}{\hbar} H + \frac{1}{2} \sum_\mu L_\mu^\dagger L_\mu - \langle L_\mu^\dagger L_\mu \rangle_{\psi_t} \right) |\psi(t)\rangle\, dt + \sum_\mu \left(\frac{L_\mu}{\langle L_\mu^\dagger L_\mu \rangle_{\psi_t}^{1/2}} - I \right) |\psi(t)\rangle\, dN_\mu(t). \tag{3.32}$$

Finally, by averaging over all trajectories and using the statistical properties of the Poisson processes, the ensemble-averaged density matrix $\rho(t)$ evolves according to the Lindblad master equation:

$$\frac{\partial \rho}{\partial t} = -\frac{i}{\hbar}[H, \rho] + \sum_\mu \left(L_\mu \rho L_\mu^\dagger - \frac{1}{2}\{L_\mu^\dagger L_\mu, \rho\} \right). \tag{3.33}$$

As previously discussed, the quantum Monte Carlo method is more than just a powerful computational algorithm and provides physical insights into the nature of open quantum systems. A multitude of experiments [8–11] have observed quantum jumps and support quantum trajectory theory.

3.3. Wiener Unraveling

The quantum jump method is fundamentally a discrete, or Poissonian, process. From the field of stochastic processes, it turns out that one can develop the *continuous* analog of the quantum jump method using the state $|\psi(t)\rangle$ [3, 12, 13].

Recall the Lindblad master equation:

$$\frac{d\rho}{dt} = -\frac{i}{\hbar}[H, \rho] + \sum_{\mu=0} L_\mu \rho L_\mu^\dagger - \frac{1}{2}\{L_\mu^\dagger L_\mu, \rho\}. \tag{3.34}$$

Similar to the previous section, we wish to simulate open quantum systems with pure states $|\psi(t)\rangle$. This entails that we understand the individual trajectories each state can take. Since the density matrix ρ represents the statistical mixture of states, the quantum dynamics of the individual states are obscured. To recover the physical interpretation of individual systems, we unravel the density matrix ρ as an ensemble of pure state trajectories, namely,

$$\rho(t) = \mathbb{E}[|\psi(t)\rangle\,\langle\psi(t)|]. \tag{3.35}$$

Due to the inherently random nature of the dynamics, each trajectory $|\psi(t)\rangle$ evolves stochastically.

For our formulation to be physically relevant, it must be able to recover the Lindblad master equation. Thus, we first seek to find the equation that governs the evolution of $|\psi(t)\rangle$. Let $|\psi(t)\rangle$ be an arbitrary pure state. Suppose that $|\psi(t)\rangle$ does not undergo a jump. Then the state $|\psi(t)\rangle$ evolves under the non-Hermitian, effective Hamiltonian

$$H_{\text{eff}} = H - i\hbar J = H - \frac{i\hbar}{2}\sum_{\mu\neq 0} L_\mu^\dagger L_\mu, \tag{3.36}$$

where H is the Hermitian Hamiltonian of the system that governs the unitary evolution. Thus, $|\psi(t)\rangle$ evolves according to

$$d\,|\psi(t)\rangle = -\frac{i}{\hbar} H_{\text{eff}}\,|\psi(t)\rangle\,dt. \tag{3.37}$$

To incorporate continuous stochastic dynamics, we must add noise terms to this evolution that reflect the system-environment interactions. From the theory of quantum state diffusion [3, 13], the Wiener unraveling is derived as follows:

$$d\,|\psi(t)\rangle = -\frac{i}{\hbar} H\,|\psi(t)\rangle\,dt + \sum_\mu \left[\langle L_\mu^\dagger\rangle_{\psi_t} L_\mu - \frac{1}{2}\left(L_\mu^\dagger L_\mu + \left|\langle L_\mu\rangle_{\psi_t}\right|^2\right)\right]|\psi(t)\rangle\,dt \tag{3.38}$$

$$+ \frac{1}{\sqrt{2}}\sum_\mu \left(L_\mu - \langle L_\mu\rangle_{\psi_t}\right)|\psi(t)\rangle\,dW_\mu(t), \tag{3.39}$$

where $dW_\mu(t)$ is a complex Wiener process satisfying

$$\mathbb{E}[dW_\mu(t)] = 0, \quad \mathbb{E}[dW_\mu(t)dW_\nu(t)] = 0, \quad \mathbb{E}[dW_\mu^*(t)dW_\nu(t)] = 2\delta_{\mu\nu}dt. \tag{3.40}$$

The first term in Eq. (3.39) represents the deterministic unitary evolution of the system under the Hermitian Hamiltonian H. The second term is the drift, which accounts for the dissipative effects encoded in the Lindblad operators L_μ. The third term is the diffusion term, which incorporates stochastic noise due to continuous measurement-like interactions between the system and its environment [6, 13].

To verify that the stochastic differential equation recovers the Lindblad master equation, we compute the ensemble average of the outer product $|\psi(t)\rangle\langle\psi(t)|$. Using the Itô calculus for stochastic processes, it can be shown that the terms in Eq. (3.39) lead to the Lindblad form for the density matrix evolution [3, 13]:

$$\frac{d\rho}{dt} = -\frac{i}{\hbar}[H,\rho] + \sum_{\mu=0} L_\mu \rho L_\mu^\dagger - \frac{1}{2}\{L_\mu^\dagger L_\mu, \rho\}. \tag{3.41}$$

This ensures the equivalence of the Wiener unraveling with the Lindblad master equation when averaged over all stochastic trajectories.

The Wiener unraveling provides a powerful and intuitive framework for studying continuous measurement processes and decoherence in quantum systems, complementing the discrete picture of the quantum jump method.

4 Schrödinger Cat States

For a review on coherent states and field oscillators, see Appendices A-B.

Schrödinger cat states are quantum superpositions of macroscopically distinct coherent states, highlighting the peculiarities of quantum mechanics such as superposition and entanglement. These states are crucial for exploring the boundary between quantum and classical regimes, particularly in quantum optics and quantum information science.

4.1. Definition and Construction of Schrödinger Cat States

A coherent state $|\beta\rangle$ in quantum optics is a minimum-uncertainty state that closely resembles a classical field. It is defined as an eigenstate of the annihilation operator $\hat{a}$:

$$\hat{a}\,|\beta\rangle = \beta\,|\beta\rangle\,, \tag{4.1}$$

where $\beta \in \mathbb{C}$ is the complex amplitude, characterizing the field's phase and intensity.

A Schrödinger cat state arises from the coherent superposition of two such states with macroscopically distinct amplitudes β_1 and β_2. The general form is:

$$|\Psi_{\text{cat}}\rangle = \frac{1}{\sqrt{\mathcal{N}}}\left(e^{i\phi_1}\,|\beta_1\rangle + e^{i\phi_2}\,|\beta_2\rangle\right), \tag{4.2}$$

where $\mathcal{N}$ is a normalization constant accounting for the overlap between $|\beta_1\rangle$ and $|\beta_2\rangle$. The overlap is given by $\langle\beta_1|\beta_2\rangle = \exp\left(-\frac{1}{2}|\beta_1 - \beta_2|^2\right)$, which becomes negligible for $|\beta_1 - \beta_2| \gg 1$. In this limit, the state simplifies to:

$$|\Psi_{\text{cat}}\rangle \approx \frac{1}{\sqrt{2}}\left(e^{i\phi_1}\,|\beta_1\rangle + e^{i\phi_2}\,|\beta_2\rangle\right). \tag{4.3}$$

A particularly interesting class of cat states is the *phase cat states*, where the coherent amplitudes β_1 and β_2 have equal magnitudes but differ in phase. For example, $\beta_1 = \beta$ and $\beta_2 = -\beta$ lead to even and odd π-phase cats:

$$|\Psi^{\pm}_{\text{cat}}\rangle = \frac{|\beta\rangle \pm |-\beta\rangle}{\sqrt{2(1 \pm e^{-2|\beta|^2})}} \approx \frac{1}{\sqrt{2}}\left(|\beta\rangle \pm |-\beta\rangle\right), \tag{4.4}$$

for $|\beta| \gg 1$. These states exhibit interference fringes in phase space, a hallmark of their quantum nature.

4.2. Properties and Applications

Schrödinger cat states exhibit highly non-classical behavior. Their Wigner functions, defined as quasi-probability distributions in phase space, often show regions of negativity, reflecting their quantum coherence. This non-classicality is instrumental in probing the quantum-to-classical transition.

Cat states are highly susceptible to decoherence due to their macroscopic superposition nature. Interaction with the environment rapidly collapses the superposition, making these

states a sensitive tool for studying decoherence mechanisms and the dynamics of open quantum systems.

Cat states have numerous applications in quantum information science. They serve as resources for fault-tolerant quantum computation in bosonic codes, such as the binomial and GKP (Gottesman-Kitaev-Preskill) codes. These states can also be used in quantum metrology to enhance precision measurements beyond the standard quantum limit.

4.3. Generalization to Multi-Component Cat States

The concept of Schrödinger cat states can be extended to superpositions involving more than two coherent states. For q equally spaced coherent amplitudes distributed around a circle in phase space, the state is given by:

$$|\Psi_q^k\rangle = \frac{1}{\sqrt{q}} \sum_{p=0}^{q-1} e^{-2\pi i k p/q} \, |\beta e^{2\pi i p/q}\rangle \,, \quad k = 0, 1, \ldots, q-1. \tag{4.5}$$

These generalized cat states exhibit rotational symmetry in phase space and have potential applications in quantum communication protocols and symmetry-protected quantum computation.

4.4. Experimental Realization

Schrödinger cat states have been realized in various platforms, including cavity quantum electrodynamics (CQED), trapped ions, and superconducting circuits. In CQED, such states are created by dispersively coupling a coherent light field to Rydberg atoms. The controlled interaction generates superpositions of coherent states with well-defined phase relationships. These experimental setups are ideal for investigating decoherence and the dynamics of macroscopic quantum superpositions.

Schrödinger cat states continue to provide profound insights into quantum mechanics and its intersection with classical physics, serving as a bridge between theoretical constructs and experimental realizations.

5 Homodyne Detection

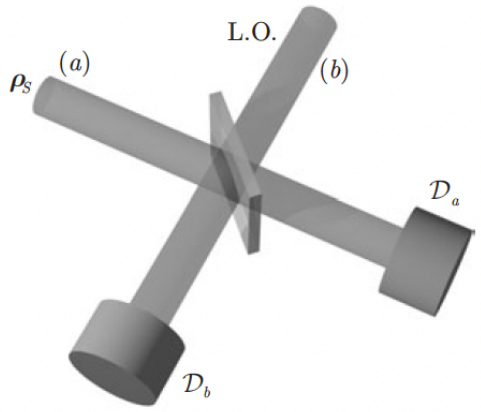

FIG. 2. Principle of homodyne detection of an unknown field with density ρ_S from [4].

Homodyne detection is a critical technique in quantum optics, allowing for the precise measurement of field quadratures and phase information in light fields. In particular, it plays a central role in experiments involving Schrödinger cat states by enabling phase-sensitive measurements. This method compares the signal field with a coherent reference beam known as the local oscillator (L.O.) to extract phase and amplitude information.

Figure 2 illustrates the principle of homodyne detection for an unknown input signal field a, described by the density operator ρ_S [4]. The L.O., denoted as b, is prepared in a coherent state $|\beta\rangle = |\beta_0 e^{i\phi}\rangle$. When the signal and L.O. beams intersect at a beam-splitter, they are mixed into transmitted and reflected components. The transmitted signal beam mixes with the reflected L.O. beam and is measured by detector $\mathcal{D}_a$, which counts photons n_a. Similarly, the transmitted L.O. beam mixes with the reflected signal beam and is measured by detector $\mathcal{D}_b$, counting photons n_b.

The mean photon counts at the detectors are given by:

$$n_a = \frac{1}{2}\mathrm{Tr}\left[\rho_S \left|\beta\right\rangle \left\langle\beta\right| \left(a^\dagger - ib^\dagger\right)(a + ib)\right], \tag{5.1}$$

$$n_b = \frac{1}{2}\mathrm{Tr}\left[\rho_S \left|\beta\right\rangle \left\langle\beta\right| \left(a^\dagger + ib^\dagger\right)(a - ib)\right]. \tag{5.2}$$

Subtracting the photon counts $n_a - n_b$ yields the difference counting signal:

$$n_a - n_b = i\beta_0 \mathrm{Tr}\left[\rho_S \left(a^\dagger e^{i\phi} - a e^{-i\phi}\right)\right] = 2\beta_0 \left\langle X_{\phi+\pi/2}\right\rangle_S. \tag{5.3}$$

This signal measures the expectation value of the field quadrature $X_{\phi+\pi/2}$, which is $\pi/2$-out-of-phase with the L.O. By sweeping the phase ϕ of the L.O., one can measure the expectation value of any field quadrature.

Homodyne detection is not limited to extracting quadrature averages. By analyzing the distribution of photocount differences across an ensemble of identically prepared fields, it is possible to reconstruct the probability distribution of the quadrature values. This provides a

complete characterization of the quantum state, enabling the reconstruction of the Wigner function W, and ultimately, the density operator ρ_S.

This method proves invaluable in experiments involving Schrödinger cat states, as it allows for the direct measurement of phase-sensitive properties and provides a window into the non-classical nature of these states [4].

6 Unraveling the Cat

6.1. Case Study: Homodyne Cat State Measurement

As discussed earlier, it is intriguing that two different unravelings can model the same physical phenomenon and converge to the same Lindblad master equation. To explore this in-depth, we present a case study applying these unravelings to Schrödinger cat states. Using a thought experiment inspired from Haroche [4] and numerical simulations, we examine the master equation unravelings and their trajectories. The thought experiment investigates how a homodyne measurement interacts with a Schrödinger cat state in a cavity, highlighting the interplay of quantum measurement, decoherence, and the evolution of mesoscopic quantum states. For our simulations, we utilize the QuTiP [14] package in Python.

Alice prepares a π-phase cat state,

$$|\Psi_{\text{cat}}^{+(A)}\rangle = \frac{|\beta\rangle + |-\beta\rangle}{\sqrt{2}}, \quad \beta \in \mathbb{R}, \tag{6.1}$$

in a cavity C_A. The cavity leaks photons at a rate κ through one of its mirrors, allowing the state to interact with its environment. Bob captures this leaking field using a symmetric beam splitter that mixes it with a reference homodyne field. This reference has a tunable amplitude and phase, enabling the measurement of specific quadratures of the cavity field. Two detectors, $\mathcal{D}_1$ and $\mathcal{D}_2$, are placed at the beam splitter's outputs to record photon counts. The environment simulator B thus has three states: $|0^{(B)}\rangle$, $|1^{(B)}\rangle$, and $|2^{(B)}\rangle$, which encode the 'no click,' 'click in $\mathcal{D}_1$,' and 'click in $\mathcal{D}_2$,' respectively.

In this setup, the beam-splitter parameters are set to $\varphi = 0$ and $\theta = \pi/2$, ensuring mode mixing as described in (D4). Under these conditions, the field transmitted toward detector $\mathcal{D}_1$ is equivalent to the field that would directly emerge from the cavity C_A if the beam splitter were absent. This equivalence holds if the cavity leaking rate is effectively halved to $\kappa/2$ and the cavity field is shifted in phase space by $i\alpha = i\xi e^{-i\phi_r}\beta$, where the factor i accounts for the phase shift introduced by the reflection of the reference field. This phase-space translation is performed by the displacement operator

$$D(i\alpha) = \exp\left(i\alpha a^\dagger - i\alpha^* a\right), \tag{6.2}$$

where a and $a^\dagger$ are the annihilation and creation operators of the cavity mode, respectively. When $\mathcal{D}_1$ registers a detection event (a "click"), the translated cavity field undergoes a jump described by the Lindblad operator:

$$L = \sqrt{\frac{\kappa}{2}}a. \tag{6.3}$$

To reflect the actual evolution of the field stored in C_A, the translation induced by $D(i\alpha)$

must be reversed. This results in the effective collapse operator:

$$L_1(\alpha) = \sqrt{\frac{\kappa}{2}} D^{-1}(i\alpha) a D(i\alpha) = \sqrt{\frac{\kappa}{2}} (a + i\alpha) . \tag{6.4}$$

Here, we expanded the displacement operator by applying the Baker-Campbell-Hausdorff formula. Similarly, for detector $\mathcal{D}_2$, the phase-space translation corresponds to $D(-i\alpha)$, leading to the collapse operator:

$$L_2(\alpha) = i\sqrt{\frac{\kappa}{2}} D^{-1}(-i\alpha) a D(-i\alpha) = i\sqrt{\frac{\kappa}{2}} (a - i\alpha) . \tag{6.5}$$

Each detection event triggers a quantum jump, progressively collapsing the cat state toward one of its coherent components, $|\beta\rangle$ or $|-\beta\rangle$. Clicks in $\mathcal{D}_1$ favor $|\beta\rangle$, while clicks in $\mathcal{D}_2$ favor $|-\beta\rangle$.

Over time, as photons leak from the cavity, the superposition evolves stochastically, with the state updated after each detection event. This process gradually reduces the coherence between $|\beta\rangle$ and $|-\beta\rangle$, transforming the superposition into a statistical mixture. The rate of decoherence is proportional to the photon number n, making it significantly faster than the classical energy decay time, $1/\kappa$. This demonstrates how environmental interactions drive decoherence, with information about the cat state leaking into the detectors.

The experiment highlights the role of homodyne measurement in probing specific quadratures of the cavity field and driving its evolution. By tuning the amplitude and phase of the reference field, Bob can access precise information about the cavity state. The collapse operators L_1 and L_2 encode the interaction between the leaking cavity field, the reference, and the detectors, emphasizing how quantum measurement induces backaction on the system.

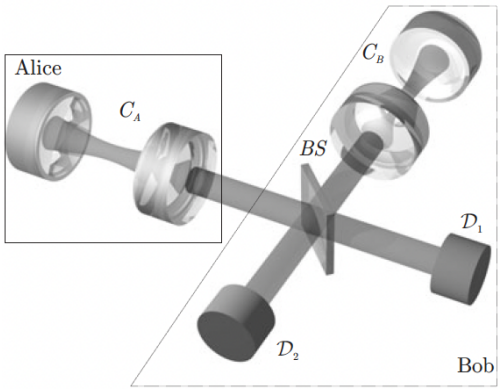

FIG. 3. Homodyne thought experiment from [4].

The observables of interest are the *parity*, *coherence*, and *photon count/number*, defined as:

$$\langle \mathcal{P} \rangle = \langle e^{i\pi a^\dagger a} \rangle , \quad \langle \mathcal{C} \rangle = |\langle a \rangle|, \quad \text{and} \quad \langle N \rangle = \langle a^\dagger a \rangle , \tag{6.6}$$

respectively. The parity tracks the even or odd photon number distribution in the cavity, serving as a measure of transitions between the cat components, $|\beta\rangle$ and $|-\beta\rangle$. This makes it a key observable for studying the coherence between the superposed states. The coherence reflects the quantum coherence of the cavity field and decays over time due to interactions

with the environment. This decay is a direct indicator of the loss of superposition and the onset of decoherence. Lastly, the photon number measures the total number of photons in the cavity, providing insight into the field's energy content.

For our simulations, we choose to set $H = 0$, simplifying the system by eliminating any unitary dynamics. This allows us to focus solely on the dissipative dynamics governed by the collapse operators, which are central to the evolution of the cavity field under homodyne detection.

6.2. The Jumping Cat: Poisson Unraveling

The explicit expression of the Poisson unraveling (3.32) with the collapse operators (6.4) and (6.5) is given by:

$$\begin{aligned} d\left|\psi(t)\right\rangle = &-\left(\frac{i}{\hbar}H + \frac{\kappa}{4}\Big[2a^\dagger a + 2\alpha^2\Big] - \kappa\Big[\left\langle a^\dagger a\right\rangle + \alpha^2\Big]\right)\left|\psi(t)\right\rangle dt \\ &+ \sum_{\mu=1,2}\left(\frac{L_\mu}{\left\langle L_\mu^\dagger L_\mu\right\rangle_{\psi_t}^{1/2}} - I\right)\left|\psi(t)\right\rangle dN_\mu(t), \end{aligned} \tag{6.7}$$

where dN_1 and dN_2 are independent Poisson processes representing the clicks in detectors $\mathcal{D}_1$ and $\mathcal{D}_2$, respectively. To implement (6.7), we use the quantum jump algorithm 1.

Let $|\phi^{(A)}\rangle$ represent the wave function at $\tau = 0$. Initially, the environment B is prepared in the vacuum state $|0^{(B)}\rangle$, resulting in:

$$\begin{aligned} \left|\phi^{(A)}\right\rangle\left|0^{(B)}\right\rangle \to &\left[1 - \frac{\tau}{2}\Big(L_1^\dagger(\alpha)L_1(\alpha) + L_2^\dagger(\alpha)L_2(\alpha)\Big)\right]\left|\phi^{(A)}\right\rangle\left|0^{(B)}\right\rangle \\ &+ \sqrt{\tau}\left[L_1(\alpha)\left|\phi^{(A)}\right\rangle\left|1^{(B)}\right\rangle + L_2(\alpha)\left|\phi^{(A)}\right\rangle\left|2^{(B)}\right\rangle\right]. \end{aligned} \tag{6.8}$$

From (6.8), we observe that the probabilities of clicks occurring in detectors $\mathcal{D}_1$ and $\mathcal{D}_2$ are given by:

$$p_1 = \tau\left\langle\phi^{(A)}|L_1^\dagger L_1|\phi^{(A)}\right\rangle = \frac{\tau\kappa}{2}\left\langle\phi^{(A)}|(a^\dagger - i\alpha^*)(a + i\alpha)|\phi^{(A)}\right\rangle, \tag{6.9}$$

$$p_2 = \tau\left\langle\phi^{(A)}|L_2^\dagger L_2|\phi^{(A)}\right\rangle = \frac{\tau\kappa}{2}\left\langle\phi^{(A)}|(a^\dagger + i\alpha^*)(a - i\alpha)|\phi^{(A)}\right\rangle, \tag{6.10}$$

respectively. The no-click case occurs with probability:

$$p_0 = 1 - p_1 - p_2. \tag{6.11}$$

These probabilities govern the stochastic evolution of the system under the Poisson unraveling, capturing the interplay between quantum measurement events and the collapse of the wave function.

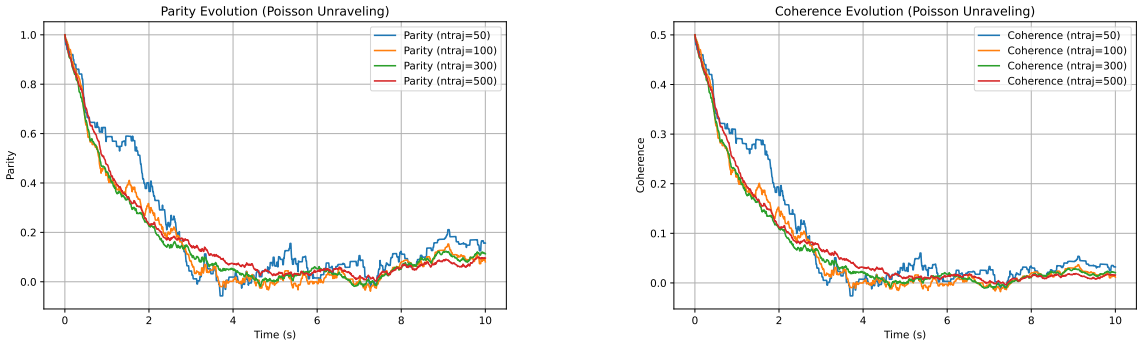

FIG. 4. Parity (left) and coherence (right) evolution under Poisson unraveling. We use $\alpha = 2$, $\kappa = 0.1$, $t_{max} = 5$, $n_{steps} = 1000$, and $dt = t_{max}/n_{steps}$ for multiple trajectories $ntraj$.

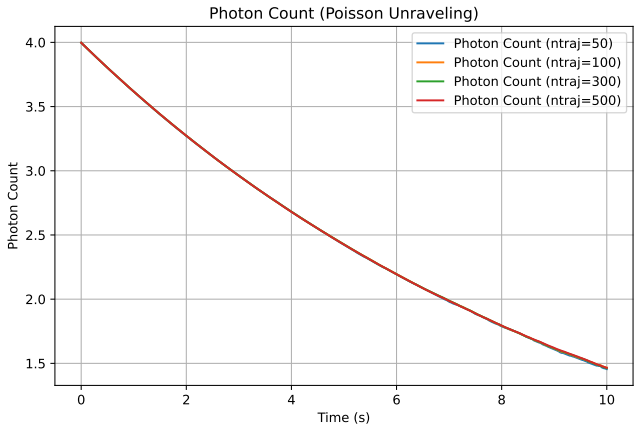

FIG. 5. Photon count under Poisson unraveling. We use $\alpha = 2$, $\kappa = 0.1$, $t_{max} = 5$, $n_{steps} = 1000$, and $dt = t_{max}/n_{steps}$ for multiple trajectories $ntraj$.

Our simulations of the Poisson unraveling yield the results shown in Figs. 4 and 5. These figures illustrate the evolution of key observables: parity, coherence, and photon count, as functions of time for multiple trajectories (n_{traj}).

In Fig. 4, the left panel shows the parity evolution, and the right panel shows the coherence evolution. As the number of trajectories ($n_{\text{traj}} = 50, 100, 300, 500$) increases, both parity and coherence quickly converge to smooth averages. The parity, which tracks transitions between the even and odd photon number states of the cavity field, starts at a maximum value and decreases as the superposition state decoheres due to photon leakage. This behavior aligns with the expected dynamics, as the detection events gradually project the state into one of its components, $|\beta\rangle$ or $|-\beta\rangle$.

Similarly, the coherence, representing the off-diagonal elements of the cavity state in the coherent-state basis, also decays over time. This decay directly reflects the loss of quantum superposition and the transition toward a statistical mixture. The convergence of coherence across trajectories demonstrates the robustness of the Poisson unraveling in capturing the decoherence process.

Fig. 5 depicts the evolution of the photon count. For all trajectories, the photon number decreases steadily with time. This is consistent with the physical nature of the experiment, where photons are continuously leaking from the cavity due to the dissipative interaction with the environment. The rate of decay corresponds to the leakage rate $\kappa = 0.1$, confirming that the quantum jump method accurately simulates the expected energy loss in the system.

In summary, the parity tracks the even/odd photon number distribution and decreases due to transitions between the cat components, $|\beta\rangle$ and $|-\beta\rangle$. The coherence reflects the quantum superposition and decays over time due to environmental interactions, illustrating the process of decoherence. The photon count steadily decreases as photons are lost from the cavity, aligning with the expected dissipative dynamics governed by the collapse operators. These results validate the effectiveness of the Poisson unraveling in modeling the stochastic dynamics of the system and align with theoretical expectations for a Schrödinger cat state under homodyne detection.

6.3. The Randomly Walking Cat: Wiener Unraveling

The explicit expression of the Wiener unraveling (3.39) with the collapse operators (6.4) and (6.5) is given by:

$$\begin{aligned} d\,|\psi(t)\rangle = \Big(-\frac{i}{\hbar}H + \frac{\kappa}{2}\Big[\,\langle a^\dagger\rangle_{\psi_t}\, a - \frac{1}{2}(a^\dagger a + \alpha^2)\Big]\Big)\,|\psi(t)\rangle\, dt \\ + \sqrt{\frac{\kappa}{2}}\Big[\Big(a + i\alpha - \langle a + i\alpha\rangle_{\psi_t}\Big)dW_1(t) \\ + i\Big(a - i\alpha - \langle a - i\alpha\rangle_{\psi_t}\Big)dW_2(t)\Big]\,|\psi(t)\rangle\,, \end{aligned} \tag{6.12}$$

where $dW_1(t)$ and $dW_2(t)$ are independent Wiener processes. The first term represents the deterministic evolution of the system, governed by the effective Hamiltonian and the collapse operator expectation values. The second term accounts for the stochastic evolution, with the Wiener increments modeling continuous fluctuations introduced by the measurement process. This equation encapsulates the continuous, diffusive nature of the Wiener unraveling, contrasting with the discrete jumps observed in the Poisson unraveling.

Our simulations of the Wiener unraveling yield the results shown in Figs. 6 and 7. These figures depict the evolution of key observables: parity, coherence, and photon count, as functions of time for multiple trajectories ($n_{\text{traj}} = 50, 100, 300, 500$).

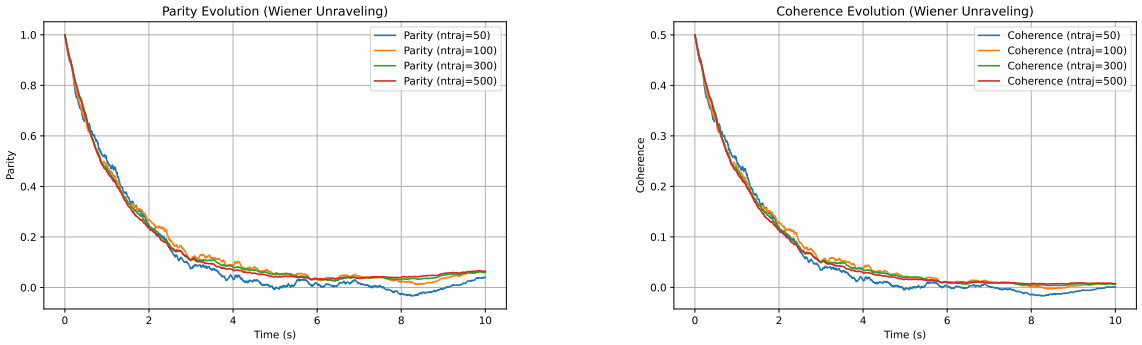

FIG. 6. Parity (left) and coherence (right) evolution under Wiener unraveling. We use $\alpha = 2$, $\kappa = 0.1$, $t_{max} = 5$, $n_{steps} = 1000$, and $dt = t_{max}/n_{steps}$ for multiple trajectories $ntraj$.

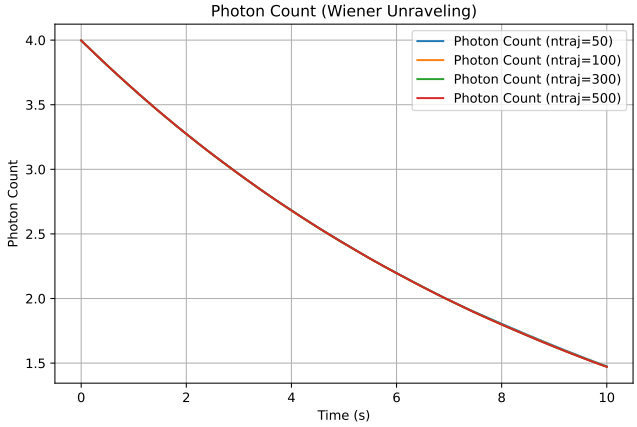

FIG. 7. Photon count under Wiener unraveling. We use $\alpha = 2$, $\kappa = 0.1$, $t_{max} = 5$, $n_{steps} = 1000$, and $dt = t_{max}/n_{steps}$ for multiple trajectories $ntraj$.

In Fig. 6, the left panel illustrates the evolution of the parity under Wiener unraveling. As the number of trajectories increases, the parity converges to smooth averages, similar to the Poisson case. However, the stochastic nature of the Wiener process introduces continuous fluctuations in individual trajectories. The parity decreases over time as the superposition state transitions toward a statistical mixture, reflecting the gradual decoherence of the system. These results are consistent with the expected dynamics of the unraveling, where the state evolves continuously without discrete quantum jumps.

The right panel of Fig. 6 shows the coherence evolution. Like the parity, the coherence also decreases over time, signifying the decay of quantum superposition due to environmental interactions. The convergence across multiple trajectories demonstrates the accuracy of the Wiener unraveling in modeling this process. The decay behavior aligns with the physical intuition that the system loses coherence as it interacts with the environment, transitioning toward a classical state.

In Fig. 7, the photon count decreases steadily with time across all trajectories. This behavior is consistent with the physical setup of the experiment, where photons are continuously leaking from the cavity due to the dissipative interaction with the environment. The rate

of decay matches the leakage rate $\kappa = 0.1$, validating the implementation of the Wiener unraveling.

In summary, the parity and coherence evolve smoothly under Wiener unraveling, with both observables showing decay consistent with the loss of superposition and the onset of decoherence. The photon count decreases steadily as photons leak from the cavity, aligning with the dissipative nature of the system. These results highlight the role of Wiener unraveling in capturing the continuous, stochastic evolution of the system's state.

6.4. Comparing the Unravelings

Before we compare the unravelings, we see that when we average over the trajectories

$$\rho(t) = \mathbb{E}\left[|\psi(t)\rangle \langle\psi(t)|\right], \tag{6.13}$$

we get the following Lindblad master equation:

$$\begin{aligned}\frac{\partial \rho}{\partial t} &= -\frac{i}{\hbar}[H,\rho] + \sum_{\mu=1}^{2} L_\mu \rho L_\mu^\dagger - \frac{1}{2}\{L_\mu^\dagger L_\mu, \rho\} \\ &= -\frac{i}{\hbar}[H,\rho(t)] + \frac{\kappa}{2}\left((a+i\alpha)\rho(a^\dagger - i\alpha^*) - \frac{1}{2}\left\{a^\dagger a + \alpha^2 + i\alpha a^\dagger - i\alpha^* a, \rho\right\}\right) \\ &+ \frac{\kappa}{2}\left((a-i\alpha)\rho(a^\dagger + i\alpha^*) - \frac{1}{2}\left\{a^\dagger a + \alpha^2 - i\alpha a^\dagger + i\alpha^* a, \rho\right\}\right),\end{aligned} \tag{6.14}$$

for both unravelings, confirming their equivalence.

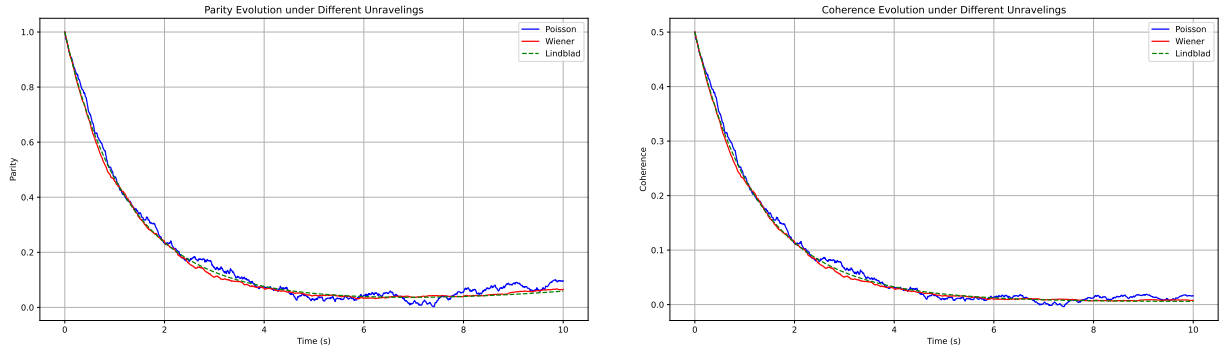

FIG. 8. Parity (left) and coherence (right) evolution under Poisson unraveling, Wiener unraveling, and Lindblad master equation. We use $\alpha = 2$, $\kappa = 0.1$, $t_{max} = 5$, $n_{steps} = 1000$, and $dt = t_{max}/n_{steps}$ for $ntraj = 500$ trajectories.

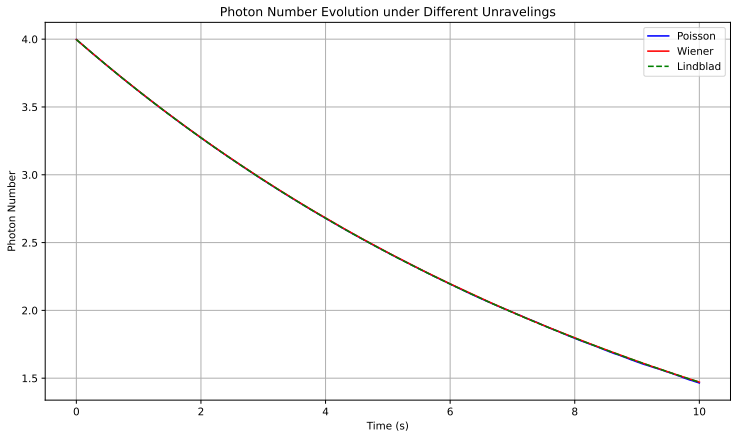

FIG. 9. Photon count under Poisson unraveling, Wiener unraveling, and Lindblad master equation. We use $\alpha = 2$, $\kappa = 0.1$, $t_{max} = 5$, $n_{steps} = 1000$, and $dt = t_{max}/n_{steps}$ for $ntraj = 500$ trajectories.

On physical grounds, we expect the photon count to exhibit the same behavior no matter the unraveling and number of trajectories used. This is clearly seen in Fig. 9, where the photon counts for both unravelings agree with each other and with the Lindblad formulation. This agreement demonstrates the equivalence of the unravelings when averaged over trajectories.

In Fig. 8, we compare the evolution of parity and coherence for the Poisson and Wiener unravelings alongside the Lindblad master equation. The parity evolution shows that both unravelings follow the same trend as the master equation, with the Poisson unraveling featuring discrete jumps due to the stochastic quantum jumps in individual trajectories, while the Wiener unraveling produces smoother trajectories due to its diffusive nature. Both unravelings average out to match the results of the Lindblad equation, validating their equivalence.

Similarly, the coherence evolution in Fig. 8 (right panel) demonstrates consistent decay across the unravelings and the master equation. The Wiener unraveling produces slightly smoother averages due to its continuous nature, whereas the Poisson unraveling reflects the discrete jumps of individual trajectories. In all cases, the coherence decreases as the system loses quantum superposition due to interactions with the environment.

In summary, both unravelings capture the same physical dynamics as described by the Lindblad master equation. The Poisson unraveling emphasizes the discrete nature of quantum measurement through jumps, while the Wiener unraveling highlights the continuous stochastic evolution of the system. Despite these differences in perspective, their ensemble-averaged results are identical and align with the Lindblad formulation.

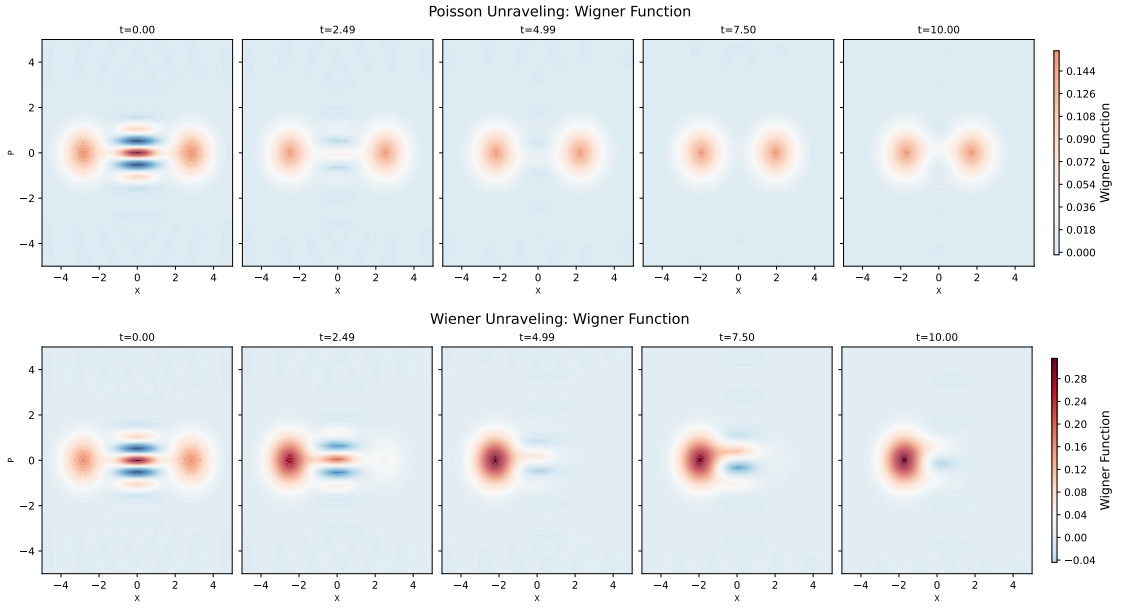

FIG. 10. Comparison of Wigner functions for Poisson (top) and Wiener (bottom) unravelings. The Poisson unraveling exhibits discrete jumps, leading to more stochastic features in the Wigner distribution, while the Wiener unraveling shows smoother transitions reflecting continuous weak measurements. Both methods recover the Lindblad equation in the ensemble average.

Perhaps the most striking feature of the unravelings is the behavior of their Wigner functions, as shown in Fig. 10. The Wigner function offers a quasi-probability distribution in phase space, allowing us to visualize the evolution of the quantum state. These plots illustrate the stark differences in how the Poisson and Wiener unravelings evolve the system over time.

The top panel of Fig. 10 depicts the Wigner function for the Poisson unraveling at various time points. The stochastic nature of quantum jumps is evident in these snapshots. Initially, the Wigner function shows high coherence, with clear interference fringes characteristic of a Schrödinger cat state. As time progresses, discrete jumps cause abrupt changes in the distribution. This manifests as a reduction in coherence, with the interference fringes fading unevenly. By $t = 10$, the Wigner function has evolved into a mixed state, reflecting the system's decoherence due to environmental interactions.

In contrast, the bottom panel shows the Wigner function for the Wiener unraveling. Unlike the Poisson unraveling, the Wiener unraveling exhibits smooth transitions in the Wigner distribution, indicative of continuous weak measurements. The initial coherence of the Schrödinger cat state is also evident here, with interference fringes in phase space. However, these fringes decay more uniformly over time compared to the Poisson unraveling. By $t = 10$, the Wigner function similarly evolves into a mixed state, but the transition is much less abrupt, highlighting the diffusive nature of the Wiener unraveling.

Both unravelings recover the Lindblad equation in the ensemble average, as seen in earlier results. However, the trajectory-level dynamics differ significantly. The Poisson unraveling emphasizes the discrete, stochastic nature of quantum jumps, while the Wiener unraveling highlights the smooth, continuous evolution under weak measurements. These differences are captured vividly in their respective Wigner function dynamics, offering complementary perspectives on the system's evolution.

7 Outlook

7.1. Discerning Between the Jump and Continuous Walk

From the Poisson and Wiener unravelings, we expect to observe distinct dynamics and statistical quantities for various physical observables, even though both unravelings average to the same Lindblad master equation. These differences are particularly evident in entropy measures such as the von Neumann entropy:

$$S_{vN}(t) = -\mathrm{Tr}(\rho \log(\rho)), \tag{7.1}$$

and the Gibbs entropy:

$$S_G(t) = -\sum_i p_i \log p_i, \tag{7.2}$$

where p_i are the eigenvalues of the density matrix ρ. Theoretically, these entropies are expected to evolve differently under the two unravelings due to the contrasting nature of discrete jumps in Poisson unraveling versus the continuous noise in Wiener unraveling [15].

The distinct characteristics of these unravelings highlight their complementary roles in modeling open quantum systems. While Poisson unraveling emphasizes the stochastic and discrete aspects of quantum jumps, Wiener unraveling offers a continuous perspective, reflecting the interplay of deterministic dynamics and stochastic noise. These differences are not merely computational artifacts; they provide insights into the nature of quantum measurement and decoherence processes.

Advances in experimental techniques, particularly those involving Schrödinger cat states, offer promising avenues to discern these theoretical differences. For instance, homodyne detection experiments can be employed to measure field quadratures with high precision, enabling direct comparisons of observable dynamics under each unraveling. By reconstructing phase-space distributions such as the Wigner function, one can assess how the stochastic properties of each unraveling influence the quantum state's evolution.

Looking forward, the study of unravelings in the context of entropy measures, Ehrenfest theorems, and phase-space dynamics presents opportunities for physically distinguishing the unravelings. We hope to devise experiments that facilitate the difference between the unravelings along these lines.

Acknowledgments

I wish to acknowledge Dr. Janek Wehr for his mentorship, guidance, and patience in this semester-long project for Math 599. His expertise in the subject was instrumental in developing the knowledge needed to produce this report.

Appendix

A Field Oscillators

Recall the quantum harmonic oscillator Hamiltonian [1, 4]:

$$H_x = \frac{P^2}{2m} + \frac{1}{2}m\omega^2 X^2. \tag{A1}$$

We introduce the characteristic units:

$$x_0 = \sqrt{\frac{\hbar}{2m\omega}}, \quad p_0 = \sqrt{\frac{m\omega\hbar}{2}}, \tag{A2}$$

and the dimensionless position and momentum operators, respectively:

$$X_0 = \frac{X}{x_0}, \quad P_0 = \frac{P}{p_0}. \tag{A3}$$

Then the Hamiltonian becomes:

$$H_x = \hbar\omega\left(P_0^2 + X_0^2\right). \tag{A4}$$

We introduce the creation and annihilation operators, respectively:

$$a^\dagger = \frac{X_0 - iP_0}{\sqrt{2}}, \quad a = \frac{X_0 + iP_0}{\sqrt{2}}, \tag{A5}$$

which obey the commutation relation:

$$[a, a^\dagger] = 1. \tag{A6}$$

It can be easily shown that:

$$X_0 = \frac{a + a^\dagger}{\sqrt{2}}, \quad P_0 = i\frac{a^\dagger - a}{\sqrt{2}}. \tag{A7}$$

Defining the number operator $N = a^\dagger a$ allows us to write the Hamiltonian as:

$$H_x = \hbar\omega\left(N + \frac{1}{2}\right). \tag{A8}$$

A similar procedure applies to the quantum treatment of the electromagnetic field. Recall that the electric field operator $\hat{E}(\mathbf{r})$ depends on the mode geometry. This motivates the introduction of dimensionless, position-independent *field quadrature operators* X_ϕ:

$$X_\phi = \frac{ae^{-i\phi} + a^\dagger e^{i\phi}}{\sqrt{2}}, \tag{A9}$$

where ϕ is the phase angle. For the phase space coordinates $\{X_\phi, X_{\phi+\pi/2}\}$, the field quadra-

tures satisfy the canonical commutation relations and Heisenberg uncertainty relation, respectively:

$$[X_\phi, X_{\phi+\pi/2}] = \frac{i}{2}, \quad \Delta X_\phi \Delta X_{\phi+\pi/2} \geq \frac{1}{4}. \tag{A10}$$

The eigenstates of orthogonal quadratures can be expanded as:

$$|x_{\phi+\pi/2}\rangle = \frac{1}{\sqrt{\pi}} \int dy\, e^{2ixy} |y_\phi\rangle\,, \tag{A11}$$

where $|y_\phi\rangle$ are the eigenstates of X_ϕ.

This formalism lays the groundwork for understanding coherent states, which are superpositions of these field quadratures with well-defined classical analogs. The connection between the field oscillators and coherent states is essential for comprehending their classical-like properties and applications in quantum optics.

B Coherent States

Coherent states are a fundamental concept in quantum mechanics, particularly in quantum optics, where they describe states of the electromagnetic field that most closely resemble classical behavior. This section provides a detailed mathematical derivation and discussion of coherent states based on their properties and defining characteristics. We follow [1, 4, 16]

B1. Definition

A coherent state $|\alpha\rangle$ is defined as the eigenstate of the annihilation operator a:

$$a\,|\alpha\rangle = \alpha\,|\alpha\rangle\,, \tag{B1}$$

where $\alpha \in \mathbb{C}$ is a complex number that characterizes the coherent state. The explicit form of $|\alpha\rangle$ in the Fock basis $\{|n\rangle\}$ is:

$$|\alpha\rangle = e^{-\frac{|\alpha|^2}{2}} \sum_{n=0}^{\infty} \frac{\alpha^n}{\sqrt{n!}} |n\rangle\,. \tag{B2}$$

Here, $|n\rangle$ represents the number states (Fock states), and the exponential prefactor ensures normalization.

B2. Normalization of Coherent States

To verify that $|\alpha\rangle$ is normalized, we compute the inner product $\langle\alpha|\alpha\rangle$:

$$\langle\alpha|\alpha\rangle = \left(e^{-\frac{|\alpha|^2}{2}} \sum_{n=0}^{\infty} \frac{(\alpha^*)^n}{\sqrt{n!}} \langle n|\right) \left(e^{-\frac{|\alpha|^2}{2}} \sum_{m=0}^{\infty} \frac{\alpha^m}{\sqrt{m!}} |m\rangle\right) \tag{B3}$$

$$= e^{-\frac{|\alpha|^2}{2}} e^{-\frac{|\alpha|^2}{2}} \sum_{n=0}^{\infty} \frac{(\alpha^*)^n \alpha^n}{n!} \tag{B4}$$

$$= e^{-|\alpha|^2} \sum_{n=0}^{\infty} \frac{|\alpha|^{2n}}{n!} \tag{B5}$$

$$= e^{-|\alpha|^2} e^{|\alpha|^2} \tag{B6}$$

$$= 1. \tag{B7}$$

Thus, $|\alpha\rangle$ is indeed a normalized state.

B3. Displacement Operator Representation

Coherent states can also be generated by applying the displacement operator $D(\alpha)$ to the vacuum state $|0\rangle$:

$$|\alpha\rangle = D(\alpha)\,|0\rangle\,, \tag{B8}$$

where the displacement operator is defined as:

$$D(\alpha) = \exp\left(\alpha a^\dagger - \alpha^* a\right). \tag{B9}$$

This operator shifts the vacuum state $|0\rangle$ to a state with a non-zero expectation value of the electric field, corresponding to the classical amplitude α.

B4. Properties of Coherent States

Coherent states minimize the uncertainty relation for the quadrature operators x and p:

$$\Delta x \Delta p = \frac{\hbar}{2}, \tag{B10}$$

where x and p are defined as:

$$x = \frac{1}{\sqrt{2}}(a + a^\dagger), \quad p = \frac{i}{\sqrt{2}}(a^\dagger - a). \tag{B11}$$

This property shows that coherent states represent the closest quantum analog to classical harmonic oscillator states.

The overlap between two coherent states $|\alpha\rangle$ and $|\beta\rangle$ is given by:

$$\langle\alpha|\beta\rangle = \exp\left(-\frac{|\alpha|^2}{2} - \frac{|\beta|^2}{2} + \alpha^*\beta\right). \tag{B12}$$

This overlap is not orthogonal unless α and β are sufficiently different, reflecting the quasi-classical nature of coherent states.

For a coherent state $|\alpha\rangle$, the expectation values of the annihilation and creation operators are:

$$\langle\alpha|a|\alpha\rangle = \alpha, \quad \langle\alpha|a^\dagger|\alpha\rangle = \alpha^*. \tag{B13}$$

The number operator $N = a^\dagger a$ has the expectation value:

$$\langle\alpha|N|\alpha\rangle = |\alpha|^2. \tag{B14}$$

The variance in the photon number is:

$$\Delta N^2 = \langle N^2\rangle - \langle N\rangle^2 = |\alpha|^2. \tag{B15}$$

This indicates that the photon number distribution in a coherent state follows a Poissonian distribution.

B5. Coherent States in Phase Space

The Wigner function for a coherent state $|\alpha\rangle$ can be derived starting from the relation:

$$|x_{\phi+\pi/2}\rangle = \frac{1}{\sqrt{\pi}} \int dy\, e^{2ixy}\, |y_\phi\rangle\,, \tag{B16}$$

where $x_{\phi+\pi/2}$ and y_ϕ are the quadratures related by the phase difference $\pi/2$. The Wigner function is defined as:

$$W(x,p) = \frac{1}{\pi} \int dy\, e^{-2ipy}\, \langle x+y|\, \rho\, |x-y\rangle\,. \tag{B17}$$

For a coherent state $\rho = |\alpha\rangle\langle\alpha|$, substituting the expression for $|\alpha\rangle$ gives:

$$W(x,p) = \frac{1}{\pi} \exp\left(-\left(x - \sqrt{2}\mathrm{Re}(\alpha)\right)^2 - \left(p - \sqrt{2}\mathrm{Im}(\alpha)\right)^2\right). \tag{B18}$$

This representation highlights the classical-like behavior of coherent states in phase space, with quantum fluctuations represented by the Gaussian width.

C Coupled Harmonic Oscillators

Recall that the electromagnetic field is modeled as field oscillators. Suppose we have two independent field oscillators with Hamiltonians H_a and H_b. Assume that both oscillators

have the same frequency ω. Then we have

$$H_a = \hbar\omega\left(a^\dagger a + \frac{1}{2}\right), \quad H_b = \hbar\omega\left(b^\dagger b + \frac{1}{2}\right), \tag{C1}$$

where $a^\dagger$ ($b^\dagger$) and a (b) are the creation and annihilation operators, respectively. Since the beam-splitter couples both oscillators, we expect an interaction term H_{ab} in the total Hamiltonian:

$$H = H_a + H_b + H_{ab}. \tag{C2}$$

To find the explicit form of H_{ab}, we turn to the classical description of two coupled mechanical oscillators. Classically speaking, the Hamiltonian consists of the sum of the kinetic energies of the a and b oscillators along with the coupling spring potential energy:

$$V_{ab} = \frac{m\omega g}{2}\left(X_a - X_b\right)^2 = \frac{m\omega g}{2}\left(X_a^2 - 2X_aX_b + X_b^2\right) = V_a + V_b - m\omega g X_a X_b, \tag{C3}$$

where X_a and X_b are the oscillator positions and g is the coupling constant. Thus the classical interaction term is

$$-m\omega g X_a X_b. \tag{C4}$$

To quantize this expression, we use the identity

$$X = \left(\frac{\hbar}{2m\omega}\right)^{1/2}, \tag{C5}$$

to get

$$H_{ab} = -\frac{\hbar g}{2}\left(a + a^\dagger\right)\left(b + b^\dagger\right). \tag{C6}$$

D Quantum Action of the Beam-Splitter

Beam-splitting experiments use a beam-splitter to couple two or more beams, allowing for photon counting and quantum interference effects. Quantitatively, these beams are modeled as field oscillators, and the beam-splitter couples two or more field oscillators. This section models the quantum action of a beam-splitter on the input state $|\Psi\rangle$, focusing on two beams for simplicity.

D1. Beam-Splitter Transformation

Suppose we have two modes a and b of a radiation field with the same frequency ω. At their intersection, a partially transmitting, partially reflecting dielectric slab inclined at 45 degrees transforms the incoming electric field amplitudes E_a and E_b into outgoing amplitudes

E'_a and E'_b via the unitary transformation:

$$\begin{pmatrix} E'_a \\ E'_b \end{pmatrix} = U_c \begin{pmatrix} E_a \\ E_b \end{pmatrix} = \begin{pmatrix} t(\omega) & r(\omega) \\ r(\omega) & t(\omega) \end{pmatrix} \begin{pmatrix} E_a \\ E_b \end{pmatrix}, \tag{D1}$$

where $t(\omega)$ and $r(\omega)$ are the transmission and reflection coefficients, respectively. These satisfy the unitarity conditions:

$$|t(\omega)|^2 + |r(\omega)|^2 = 1, \quad t(\omega)r^*(\omega) + t^*(\omega)r(\omega) = 0. \tag{D2}$$

Choosing the phase origin such that $t(\omega)$ is real and positive and $r(\omega)$ is purely imaginary, we define $t(\omega) = \cos(\theta/2)$ and $r(\omega) = i\sin(\theta/2)$. The transformation becomes:

$$U_c = \begin{pmatrix} \cos(\theta/2) & i\sin(\theta/2) \\ i\sin(\theta/2) & \cos(\theta/2) \end{pmatrix}. \tag{D3}$$

Including phase shifts $\pm\varphi$ introduced by phase-retarding plates, the transformation generalizes to:

$$U_c(\theta,\varphi) = \begin{pmatrix} e^{i\varphi} & 0 \\ 0 & 1 \end{pmatrix} \begin{pmatrix} \cos(\theta/2) & i\sin(\theta/2) \\ i\sin(\theta/2) & \cos(\theta/2) \end{pmatrix} \begin{pmatrix} e^{-i\varphi} & 0 \\ 0 & 1 \end{pmatrix} = \begin{pmatrix} \cos(\theta/2) & ie^{i\varphi}\sin(\theta/2) \\ ie^{-i\varphi}\sin(\theta/2) & \cos(\theta/2) \end{pmatrix}. \tag{D4}$$

D2. Interaction Hamiltonian and Heisenberg Picture

The interaction Hamiltonian couples the two field oscillators transiently during a finite time interval τ, corresponding to the wave packets' simultaneous passage through the beam-splitter:

$$H_{ab}(t) = -\frac{\hbar g(t)}{2}\left(e^{-i\varphi}ab^\dagger + e^{i\varphi}a^\dagger b\right), \tag{D5}$$

where $g(t)$ is a slowly varying real coupling constant. The coupling is adiabatically switched on and off during τ.

In the Heisenberg picture, the beam-splitter transforms the input operators a and b into the output operators a' and b' via the unitary transformation:

$$a' = U^\dagger a U, \quad b' = U^\dagger b U, \tag{D6}$$

where

$$U(\theta,\varphi) = e^{-iG(\varphi)\theta/2}, \quad G(\varphi) = -\left(e^{-i\varphi}ab^\dagger + e^{i\varphi}a^\dagger b\right). \tag{D7}$$

Using the Baker-Hausdorff lemma and commutation relations, the transformed operators are:

$$a' = \cos(\theta/2)a + ie^{i\varphi}\sin(\theta/2)b, \tag{D8}$$

$$b' = ie^{-i\varphi}\sin(\theta/2)a + \cos(\theta/2)b. \tag{D9}$$

Combining a and b into a vector $\mathbf{c} = (a, b)^T$, the transformation becomes:

$$\mathbf{c}' = U_c \mathbf{c}. \tag{D10}$$

D3. Schrödinger Picture and State Transformation

In the Schrödinger picture, the beam-splitter acts on the input state $|\Psi\rangle$ to produce the output state $|\Psi'\rangle$:

$$|\Psi'\rangle = U |\Psi\rangle . \tag{D11}$$

For the vacuum state $|\Psi\rangle = |0, 0\rangle$, the output remains unchanged:

$$U |0, 0\rangle = |0, 0\rangle . \tag{D12}$$

For a single photon in mode a, $|\Psi\rangle = |1, 0\rangle$, the output is:

$$U |1, 0\rangle = \cos(\theta/2) |1, 0\rangle + ie^{-i\varphi} \sin(\theta/2) |0, 1\rangle . \tag{D13}$$

Similarly, for a single photon in mode b, $|\Psi\rangle = |0, 1\rangle$:

$$U |0, 1\rangle = ie^{i\varphi} \sin(\theta/2) |1, 0\rangle + \cos(\theta/2) |0, 1\rangle . \tag{D14}$$

For n photons in mode a, $|\Psi\rangle = |n, 0\rangle$, the output state is:

$$U |n, 0\rangle = \sum_{p=0}^{n} \binom{n}{p}^{1/2} \cos^{n-p}(\theta/2) \left(ie^{-i\varphi} \sin(\theta/2)\right)^p |n - p, p\rangle . \tag{D15}$$

For n photons in mode b, $|\Psi\rangle = |0, n\rangle$, the output state is:

$$U |0, n\rangle = \sum_{p=0}^{n} \binom{n}{p}^{1/2} \left(ie^{i\varphi} \sin(\theta/2)\right)^{n-p} \cos^p(\theta/2) |p, n - p\rangle . \tag{D16}$$

These results show that the beam-splitter creates entangled states for single or multiple photons, illustrating its central role in quantum optics and quantum information science.

[1] J. J. Sakurai and J. Napolitano, *Modern quantum mechanics* (Cambridge University Press, 2020).
[2] J. D. Jackson, *Classical Electrodynamics* (Wiley, 1998).
[3] H.-P. Breuer and F. Petruccione, *The theory of open quantum systems* (Oxford University Press, USA, 2002).
[4] S. Haroche and J.-M. Raimond, *Exploring the Quantum: Atoms, Cavities, and Photons* (Oxford University Press, 2006).
[5] A. J. Daley, Quantum trajectories and open many-body quantum systems, Advances in Physics **63**, 77 (2014).
[6] J. Dalibard, Y. Castin, and K. Mølmer, Wave-function approach to dissipative processes in quantum optics, Physical Review Letters **68**, 580 (1992).
[7] D. Keys and J. Wehr, Poisson stochastic master equation unravelings and the measurement problem: A quantum stochastic calculus perspective, Journal of Mathematical Physics **61**, 032101 (2020).
[8] W. Nagourney, J. Sandberg, and H. Dehmelt, Shelved optical electron amplifier: Observation of quantum jumps, Physical Review Letters **56**, 2797 (1986).
[9] T. Sauter, W. Neuhauser, R. Blatt, and P. E. Toschek, Observation of Quantum Jumps, Physical Review Letters **57**, 1696 (1986).
[10] J. C. Bergquist, R. G. Hulet, W. M. Itano, and D. J. Wineland, Observation of Quantum Jumps in a Single Atom, Physical Review Letters **57**, 1699 (1986).
[11] Z. K. Minev, S. O. Mundhada, S. Shankar, P. Reinhold, R. Gutiérrez-Jáuregui, R. J. Schoelkopf, M. Mirrahimi, H. J. Carmichael, and M. H. Devoret, To catch and reverse a quantum jump mid-flight, Nature **570**, 200 (2019).
[12] N. Gisin and I. C. Percival, The quantum-state diffusion model applied to open systems, Journal of Physics A: Mathematical and General **25**, 5677 (1992).
[13] N. Gisin and I. C. Percival, The quantum state diffusion picture of physical processes, Journal of Physics A: Mathematical and General **26**, 2245 (1993).
[14] J. Johansson, P. Nation, and F. Nori, QuTiP 2: A Python framework for the dynamics of open quantum systems, Computer Physics Communications **184**, 1234 (2013).
[15] D. Keys and J. Wehr, Nonlinear functionals of master equation unravelings (2024), arXiv:2402.05352.
[16] R. J. Glauber, Coherent and Incoherent States of the Radiation Field, Physical Review **131**, 2766 (1963), publisher: American Physical Society.